

Characterization of a silicon nanowire-based cantilever air-flow sensor

This article has been downloaded from IOPscience. Please scroll down to see the full text article.

2012 J. Micromech. Microeng. 22 095008

(<http://iopscience.iop.org/0960-1317/22/9/095008>)

View [the table of contents for this issue](#), or go to the [journal homepage](#) for more

Download details:

IP Address: 137.132.250.14

The article was downloaded on 27/07/2012 at 03:54

Please note that [terms and conditions apply](#).

Characterization of a silicon nanowire-based cantilever air-flow sensor

Songsong Zhang¹, Liang Lou¹, Woo-Tae Park² and Chengkuo Lee¹

¹ Department of Electrical and Computer Engineering, National University of Singapore, 4 Engineering Drive 3, Singapore 117576

² Department of Mechanical and Automotive Engineering, Seoul National University of Science and Technology, Seoul, Korea

E-mail: elelc@nus.edu.sg and wtpark@alumni.stanford.edu

Received 31 January 2012, in final form 13 June 2012

Published 26 July 2012

Online at stacks.iop.org/JMM/22/095008

Abstract

Silicon nanowire (SiNW)-based cantilever flow sensors with three different cantilever sizes (10×50 , 20×90 and $40 \times 100 \mu\text{m}^2$) and various SiNW lengths (2, 5 and $10 \mu\text{m}$) have been designed for air velocity sensing. The total device thickness is around $3 \mu\text{m}$, which consists of the bottom SiO_2 layer ($0.5 \mu\text{m}$) and the top SiN_x layer ($2.5 \mu\text{m}$). In addition, the SiN_x layer is used to compensate the initial stress and also enhance the device immunity to air-flow-induced vibrations significantly. To experience the maximum strain induced by the air flow, SiNWs are embedded at the clamp point where the cantilever is anchored to the substrate. Taking advantage of the superior properties of SiNWs, the reported flow sensor shows outstanding air-flow-sensing capability in terms of sensitivity, linearity and hysteresis. With only a supply voltage of 0.1 V and the high initial resistance of the piezoresistive SiNWs, significant energy saving is reached in contrast to the thermal-based flow sensors as well as other recently reported piezoresistive designs. Last but not least, the significant size reduction of our device demonstrates the great scalability of SiNW-based flow sensors.

(Some figures may appear in colour only in the online journal)

1. Introduction

Flow sensors have attracted much attention due to their various applications such as weather predictions and automotive applications. As micro-electro-mechanical systems (MEMS) technology progresses in terms of lower manufacturing cost and miniaturized dimension, the MEMS-based flow sensor not only fulfills the market demands for the traditional sensing purpose [1], but has also been successfully implemented into biomedical applications [2–4]. In 1974, the first MEMS flow sensor was introduced based on the thermal sensing mechanism [5]. Depending on the different thermal sensing principles, this mechanism can be categorized into three types: thermal anemometers, calorimetric flow sensors and time-of-flight flow sensors [6]. In general, the thermal sensing mechanism provides excellent sensitivity [7–11] and fast response time [9–13]. However, for most thermal flow sensors, the extent of improvements for these parameters is always proportional to their increased input power. Therefore, one of the common problems for such a thermal-

based flow sensor is its high power consumption. In addition, extra heat dissipation is generated through the heat convection from the heating element to the device substrate or through the air. Thus, thermal insulation becomes an important aspect for thermal sensor design to prevent extra heat loss. Numerous methods have been tried out over the past decades to refine the design required to incorporate thermal insulation. For instance, changing doping profile [14], implementing a low thermal-conductivity layer [13, 15, 16], using a freestanding structure [8, 11] and applying a vacuum cavity beneath the heating structure [17–19] have been demonstrated as methods for improving thermal insulation by various research groups in their flow sensor designs. However, due to the intrinsic power scavenging nature, the total power consumption for most thermal air-flow sensors is still above 1 mW [9, 20–25]. For liquid flow sensing, the power consumption can be even higher [23]. In addition, compromised by the high sensing resolution, the sensing range is always limited for many thermal flow sensor designs [10, 25]. To overcome this drawback, Svedin *et al* reported a

flow sensor with the combination of two mechanisms [26]. The thermal sensing scheme was used for lower flow rate detection, while the piezoresistive sensing scheme was applied for higher flow rate sensing. In the piezoresistive sensing scheme, the sensing structure will be deformed by flow-induced mechanical force, i.e. lift force [26, 27], shear force [28, 29], drag force [30–32] and even the pressure difference [33]. As a result of the mechanical deformation, strain change will be experienced by the piezoresistor. Consequently, the strain-induced piezoresistance changes are recorded by the corresponding voltage change across the piezoresistor. In this sensing scheme, the piezoresistive element is designed to be located at the anchor point between the flexible structure and the fixed device substrate. This will allow the piezoresistor to experience the maximum strain and therefore the largest piezoresistance change. Benefiting from the design simplicity, the cantilever beam is one of the popular mechanical structures, which is commonly used in the MEMS sensor designs [34–40]. In the case of a cantilever-based piezoresistive flow sensor, the piezoresistive sensing element is embedded at the fixed end of the suspended cantilever clamped on the substrate. Thus, the flow-induced cantilever deflection will be ultimately transferred to piezoresistance changes.

The earliest design of such a flow sensor was reported in the 1990s [31]. In 2000, by applying the concept of wind receptor of hairs, a 2-DOF (degree-of-freedom) flow sensor with four piezoresistive sensing elements at the base was introduced [32]. Both flow direction detection and flow velocity sensing were successfully demonstrated. By increasing the cantilever length and narrowing down the supporting beam, Su *et al* explored the relationship between the device sensitivity and its effective sensing area [41]. Inspired by the biological hair cell, Fan *et al* and Chen *et al* developed cantilever-based piezoresistive flow sensors with a vertical cilium, which was able to transfer the mechanical bending momentum from the vertical to the horizontal direction [42, 43]. Through manipulation of the residual stress, a pre-curved piezoresistive cantilever flow sensor was reported by Lee *et al* with the highest sensitivity up to $0.0284 \Omega \text{ m}^{-1} \text{ s}^{-1}$ [44]. After 2 years, the same group improved their design with maximum sensitivity to $0.0785 \Omega \text{ m}^{-1} \text{ s}^{-1}$ [45]. In 2009, an all-polymer-based air-flow sensor with sensitivity up to $66 \Omega \text{ m}^{-1} \text{ s}^{-1}$ was designed [46] and similar work has recently been modified with an external amplification at a gain of 6 [47]. To date, cantilever-based piezoresistive flow sensors have been well developed in terms of flow-sensing performance and fabrication technology, but due to the limitation of materials used as piezoresistive sensing elements, i.e. Pt strain gauge and elastomer, these recent works are not fabricated with CMOS-compatible processes [44–47]. Consequently, the electrical circuit integration becomes a potential challenge at the wafer level. Li *et al* recently reported a monolithic integrated piezoresistive cantilever flow sensor [48]. With doped bulk silicon wire as a piezoresistor, an instrumental amplification circuit with a gain of 6.5 was successfully integrated with its MEMS flow sensor at the wafer level. Except for the advantage of the CMOS compatible process, nevertheless,

this monolithic fabricated flow sensor with bulk silicon piezoresistor did not show any remarkable performances in terms of device sensitivity and linearity. In addition, the device dimension is rather bulky and would consume relatively high power. Therefore, maintaining a CMOS compatible fabrication process, meanwhile improving the device flow-sensing capability and scalability, has become a challenging topic.

In this paper, we present a silicon nanowire (SiNW)-based cantilever air-flow sensor and the device is fabricated on the (1 0 0) SOI wafer with a CMOS-compatible process. Compared to the traditional metal strain gauge and polysilicon material, the outstanding piezoresistive performance of single crystal silicon has been reported by many research groups [49–51]. The effect of giant gauge factor is still debatable [52], but migrating from bulk silicon wires to SiNWs will increase the initial piezoresistance, thus, a lower power consumption at a given supply voltage. Furthermore, the scalability of the device will be significantly improved and such improvement has been demonstrated in many modern MEMS sensor designs [53, 54].

SiNWs in three different lengths (2, 5 and $10 \mu\text{m}$) with the same average cross section of $90 \text{ nm} \times 90 \text{ nm}$ are used as the piezoresistive sensing element. By leveraging the piezoresistive effect of SiNWs, significant improvements of flow-sensing performance in terms of sensitivity, linearity and hysteresis are reported. In addition, the ultralow input power (less than $1 \mu\text{W}$) can be achieved due to the high piezoresistance ($> 150 \text{ k}\Omega$) and low supply voltage (0.1 V) used in the experiment. Additionally, the design optimization is also carried out with three different effective sensing areas ($10 \times 50, 20 \times 90, 40 \times 100 \mu\text{m}^2$) and various lengths of SiNWs.

2. Flow sensor design

2.1. Flow-sensing principle

For previously reported cantilever-based piezoresistive flow sensor designs, the flow-induced mechanical force is loaded on the cantilever structure and results in piezoresistance changes. Such mechanical force is highly dependent on the flow direction, velocity, channel dimension and the nature of the fluid. Based on the flow viscosity and velocity, the status of the flow can be defined in laminar, turbulence or transition regimes which are characterized by the Reynolds number (R_e) as shown below:

$$R_e = \frac{\rho VL}{\mu} = \frac{VL}{\nu}, \quad (1)$$

where ρ is the density of the fluid, L is the characteristic linear dimension (or diameter (d) in the case of the bounded pipe), V is the mean velocity of the object relative to the fluid, μ is the dynamic viscosity of the fluid and ν is the kinematic viscosity defined as μ/ρ . However, regardless of the laminar and turbulent flow, dependent on the channel dimension, flows can also be categorized by their boundary, i.e. internal or bounded by walls and external or unbounded [55]. As shown in the SEM picture (figure 1), in our SiNW-based cantilever air-flow sensor design, the air flow is confined within a channel

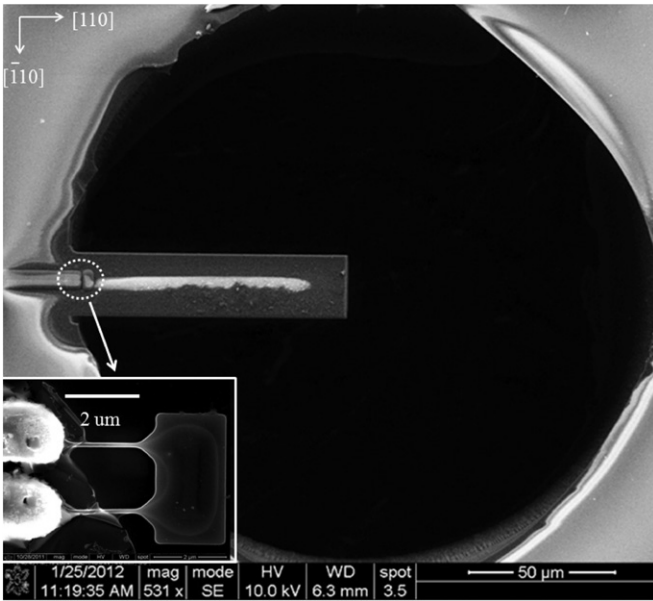


Figure 1. The SEM image of the SiNW-based cantilever flow sensor (cantilever size is $20 \mu\text{m} \times 90 \mu\text{m}$ with the SiNW length of $2 \mu\text{m}$). The inset shows the $2 \mu\text{m}$ SiNWs after etching back the top passivation layers.

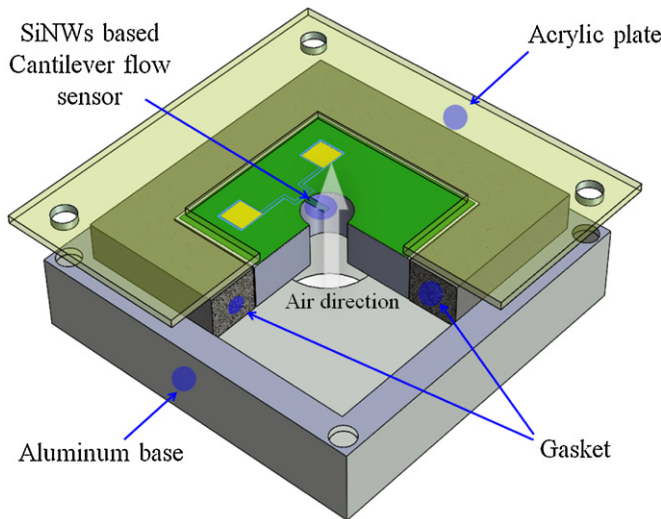


Figure 2. The schematic drawing of the SiNW-based cantilever flow sensor together with its test jig for a hermetic seal. The thick arrow indicates the air-flow direction.

of $400 \mu\text{m}$ length with a diameter of $200 \mu\text{m}$. Figure 2 shows the overall view of the device and indicates the flow direction by the thick gray arrow. In our design, the internal situation is applied instead of the external situation, but similar to the external situation, the velocity and boundary layer profiles need to be considered first. Figure 3 illustrates both the flow velocity and pressure profiles for a long pipe flow [55]. At the entrance region of the pipe, where the fluid (air in our case) flows from relatively open space into a more confined tube, the viscous boundary layers grow downstream, retarding in the vertical direction at the pipe wall and thereby accelerating

the center-core flow to maintain the incompressible continuity requirement:

$$Q = \int u \, dA = \text{constant}, \quad (2)$$

where Q is the total flow rate, u is the local flow velocity and A is the pipe cross-section area. At a given distance (L_d) from the entering point, the boundary layers merge with each other and the inviscid core disappears. Thus, the flow is said to be fully developed and the velocity is fixed. The dimensional analysis shows that the Reynolds number is the only parameter affecting the flow development length. If

$$L_d = f(d, V, \rho, \mu) \quad \text{and} \quad V = \frac{Q}{A},$$

then

$$\frac{L_d}{d} = g(\rho V d / \mu) = g(Re). \quad (3)$$

For laminar flow, the accepted correlation is

$$\frac{L_d}{d} \approx 0.06 Re. \quad (4)$$

In turbulent flow, the boundary layer grows faster and L_d is relatively shortened as

$$\frac{L_d}{d} \approx 0.06 Re^{1/6}. \quad (5)$$

With the maximum flow velocity of 65 m s^{-1} in our case, according to (1), the Reynolds number is approximately 870, which is definitely in the laminar flow regime ($Re < 2300$). After applying (4), L_d/d is calculated to be 52. Therefore, the distance required for the full development of flow is around $10400 \mu\text{m}$, which is much longer than the physical channel length ($400 \mu\text{m}$) in our actual design. Since the actual distance is significantly shorter than the distance required for air flow to be fully developed, an assumption is proposed that the air is uniformly flowing through the channel from the entry point to the cantilever surface. Thus, the pressure drop along the channel is negligible. Based on this assumption, instead of the drag force caused by viscous fluids, uniform pressure is loaded on the cantilever beam. According to [56], the equation of cantilever tip deflection (δ_{max}) is defined as

$$\delta_{\text{max}} = \frac{\omega l^4}{8EI}, \quad (6)$$

where ω is the uniformly distributed load, l is the length of the cantilever, E is Young's modulus and I is the moment of inertia,

$$I = \frac{wt^3}{12}. \quad (7)$$

Here, w is the width of the cantilever beam and t is the thickness of the cantilever. To verify the assumption of uniform pressure loaded on the cantilever, the validation test will be discussed in section 4.2.3.

2.2. Resonant frequency

The resonant frequency is another major concern for the piezoresistive-based cantilever air-flow sensor design [41]. The fundamental resonant frequency is usually required above

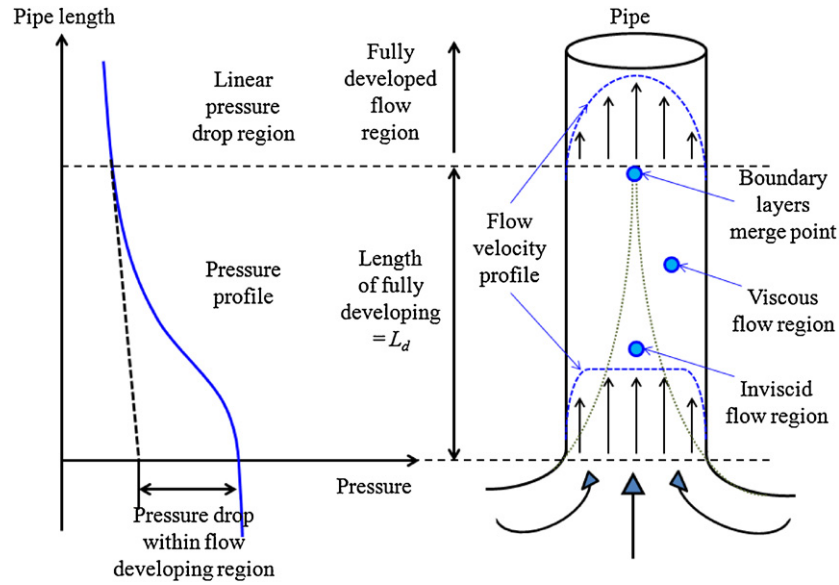


Figure 3. The illustration of flow development for internal situation.

Table 1. Comparison of resonant frequency for different combinations of materials and different cantilever sizes.

Combinations of passivation	Resonant frequency (kHz)			Cantilever size (μm^2)
	First	Second	Third	
0.5 μm SiO_2	308	1930	2993	10 \times 50
2.5 μm SiO_2	923	2994	5697	10 \times 50
2.5 μm SiN_x	1205	4261	7450	10 \times 50
0.5 μm SiO_2	95	596	896	20 \times 90
2.5 μm SiO_2	285	1781	1864	20 \times 90
2.5 μm SiN_x	373	2328	2611	20 \times 90
1 μm SiO_2	67	371	420	40 \times 100
2.5 μm SiO_2	232	1254	1447	40 \times 100
2.5 μm SiN_x	304	1592	1895	40 \times 100

10 kHz to avoid environmental excitation. Theoretically, the resonant frequency (f) of the cantilever is defined as

$$f = \frac{1}{2\pi} \sqrt{\frac{k}{m}}, \quad (8)$$

where k is the spring constant and m is the mass of the cantilever. However, the mass is hard to manipulate, especially when the device shrinks down to the micrometer scale. The optimization of the spring constant is more feasible,

$$k = \frac{Ew}{4} \frac{t^3}{l^3}. \quad (9)$$

Based on the above equation, the spring constant can be improved by either varying the cantilever geometry or changing to material with higher Young's modulus. Here, two different materials (SiO_2 and SiN_x) are selected as the passivation materials and three different cantilever size variations are explored. The FEM modeling is conducted based on these parameter combinations. The results are listed in table 1.

As shown in table 1, the resonant frequency is proportional to the cantilever thickness and inversely proportional to its effective sensing area as predicted from (9). Compared to SiO_2 , the passivation layer of SiN_x provides almost 30%

improvement of resonant frequency with a fixed geometry factor. This is contributed by the higher Young's modulus (around 170 GPa) of the SiN_x [57]. Although SiO_2 results in a low spring constant, on the other hand, the pure SiO_2 fabricated cantilever shares the merit of higher sensitivity due to its relatively low Young's modulus around 60 GPa [58].

However, such a cantilever suffers high initial deflection issues due to the large compressive stress [58] and may even result in a cantilever broken during the releasing process. Thus, the tradeoff is made between device sensitivities and initial deflection issues. As a result, the nitride layer is used to compensate internal compressive stress induced by the underlying SiO_2 layer. The details of device fabrication will be described in the following section.

3. Device fabrication

The device is fabricated on a (100) plane SOI wafer with the estimated doping level of $1.5 \times 10^{15} \text{ cm}^{-3}$ (deduced from the nominal resistivity, which is in the range from 8.5 to 11.5 $\Omega \text{ cm}$). The device layer is 117 nm and the buried oxide (box) layer is 145 nm as depicted in figure 4(a). To increase the visibility during the inspection, a 320 nm thick photoresist (model: JSR M221Y) with BARC (model: AR3-600) is coated on the wafer. Followed by the first photolithography carried out by the Nikon scanner (model: 203B), the SiNW is formed in the (110) crystal orientation with an initial width of 160 nm (figure 4(b)). Then the photoresist is trimmed for 60 s by the plasma-induced feeding gas ($\text{He}/\text{O}_2 + \text{N}_2$) and the critical dimension is approximately reduced to 110 nm. After reactive ion etching (RIE) for SiNW formation, the photoresist ashing ($\text{O}_2 + \text{N}_2$ at 250 $^\circ\text{C}$) is performed for 2 min. DHF (1:100) and Piranha cleaning are carried out to remove the etching residue and the organic residue, respectively. Sequentially, thermal dry oxidation (at 875 $^\circ\text{C}$ for 120 min) is conducted to further shrink the dimensions of SiNW s. As a result, a SiNW with an average cross section

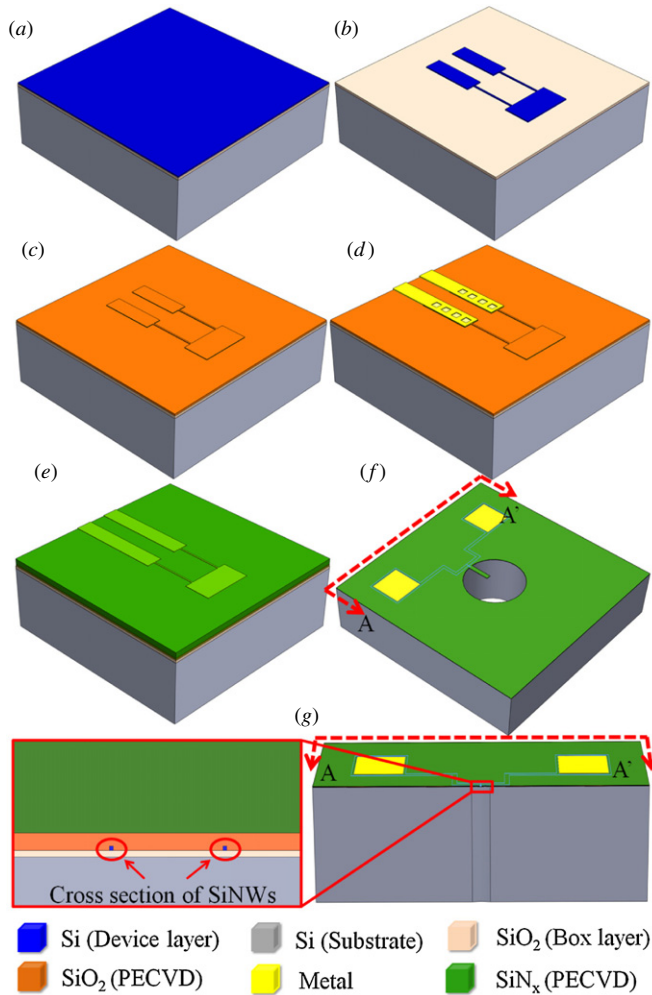


Figure 4. Illustrations of device fabrication: (a) the SOI wafer in the (100) plane; (b) SiNW formation and P-type implantation; (c) second P-type implantation on paddle regions and the first passivation layer (400 nm of SiO₂) deposition by PECVD; (d) via open, last implantation on via regions and the metallization; (e) second passivation layer (2.5 μm of SiN_x) deposition by PECVD; (f) backside release and front side cantilever structure formation by FIB; (g) cross-section view of the device with zoom-in view of the nanowire portion.

of 90 nm × 90 nm and various lengths (2, 5 and 10 μm) is finally achieved. In order to maximize the piezoresistive effect in the (1 1 0) direction [59], the P-type implantation using BF₂⁺ is performed only at nanowire regions with a dosage of 1 × 10¹⁴ ions cm⁻² and an energy of 55 keV (tilt 7° and twist 22°). The second P-type implantation is performed at the three paddle regions (two in longitudinal and one in transverse directions), which are used to connect two nanowires and form an electrical signal path as indicated in figures 4(b)–(e). The dosage level is 1 × 10¹⁵ ions cm⁻² and the implantation energy is 35 keV (tilt 7° and twist 0°). After two implantations, the dopants are activated by rapid thermal annealing (RTA) at 1000 °C for 30 s and the estimated doping concentration along the nanowire region is around 3.5 × 10¹⁸ cm⁻³. Then 0.4 μm plasma-enhanced chemical vapor deposition (PECVD at 400 °C) SiO₂ is coated as the first passivation layer (figure 4(c)) with the internal compressive stress in the range of

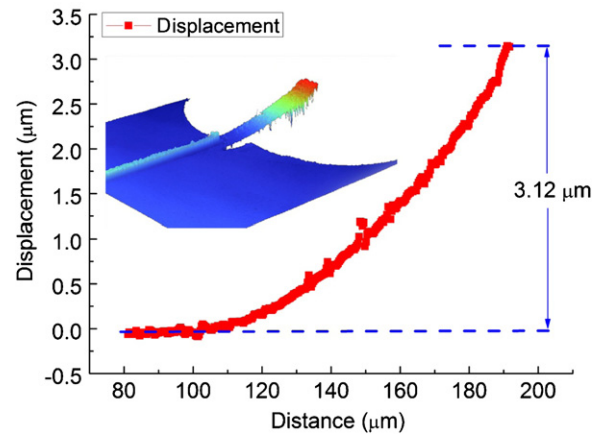


Figure 5. Plot of the initial deflection of the flow sensor with the cantilever size of 20 μm × 90 μm. The inset shows the surface profile picture captured by a white-light interferometer (Veeco NT3300) system.

250 MPa. After via open along two longitudinal paddle regions (shown in figure 4(d)), the last P-type BF₂⁺ ion is implanted with a dosage of 2 × 10¹⁵ ions cm⁻² and an energy of 35 keV (tilt 7° and twist 0°). After the same RTA step, the estimated doping concentration at the via opening region is around 1 × 10²⁰ cm⁻³. In addition, good ohmic contact between metal traces and nanowires is also ensured by measuring the contact resistance on the Kelvin structure, which is fabricated through the same process and on the same wafer. In the next step, a HF dip (10 s) is performed to remove the residue at the via opening region. A 25 nm TaN layer and 750 nm AlSiCu layer are sequentially deposited by PVD and selectively etched to form the electrical feedbacks from nanowires to bond pads (figure 4(d)). After metallization, the second passivation of the 2.5 μm low-stress silicon nitride layer (tensile stress of 100–150 MPa) is coated (PECVD at 350 °C) as shown in figure 4(e). Consequently, the device immunity of the air-flow-induced vibration is significantly enhanced (discussed in section 2.2) and the residual stress has also been minimized. Next, wafer backside grinding and polishing are carried out and the flow channel is created by backside deep reactive ion etching (DRIE) up to the BOX layer. Eventually, the front side cantilever structure is etched and defined by the focus ion beam (FIB). The final device is shown in figure 4(f). The cross-section view of both the flow sensor and cantilever is illustrated in figure 4(g). For the fully released cantilever with an area of 20 × 90 μm², the initial deflection of 3.12 μm is recorded by a white-light interferometer (Veeco NT3300) system and plotted in figure 5.

4. Device testing and experimental results

4.1. Testing setup

The test is conducted at room temperature (25 °C) with the supply voltage as low as 0.1 V to prove the proper device functionality under ultralow power. As depicted in figure 6, the compressed air is directed through the flow meter, which controls the flow rate changes. Before air reaches the aluminum

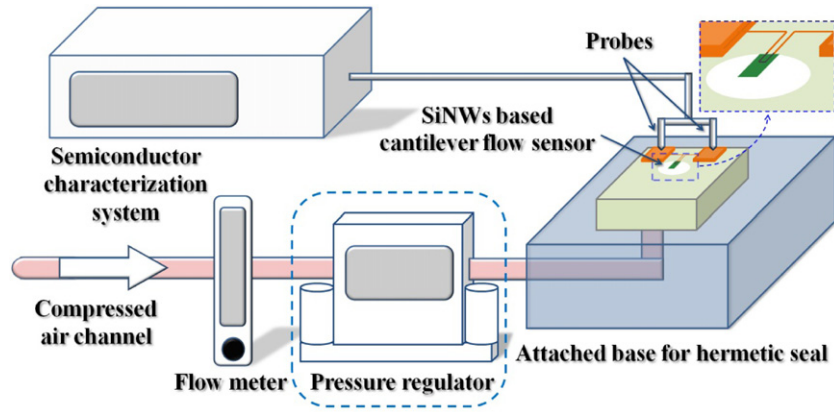


Figure 6. Testing setup for the SiNW-based cantilever air-flow sensor.

base for a hermetic seal, a pressure regulator (ALICAT PCD series) is placed in between to measure the air pressure feedback from the air channel. Based on the assumption made in section 2.1, this read back pressure is supposed to be the same amount as the uniform load applied on the cantilever beam. The semiconductor characterization system (Keithley 4200-SCS) is used to measure the piezoresistance variation with respect to the change in flow velocity. To avoid incorrect feedback readings caused by air leakage, the hermetic sealing jig is applied (shown in figure 2). The device is slotted into an aluminum base. A gasket is used to encapsulate the device and the air is confined only within the flow channel. An acrylic plate covers the top of the device with an opening window available for the passing air-flow and signal probing. Screws at each corner attach the acrylic plate to the aluminum base and tighten the sealing gasket surrounding the device body.

4.2. Testing results

4.2.1. Effect of cantilever dimension variations on the SiNW-based flow sensor: As mentioned before, devices with three different sizes (10×50 , 20×90 and $40 \times 100 \mu\text{m}^2$) are fabricated. Their SEM pictures are given in figure 7. In this section, the length of SiNWs embedded in all cantilevers is fixed to $5 \mu\text{m}$ (shown in the inset of figure 7). Similar testing regarding the effect of geometry variations has been demonstrated before and the device sensitivity was reported proportional to its effective sensing area (cantilever size) [44].

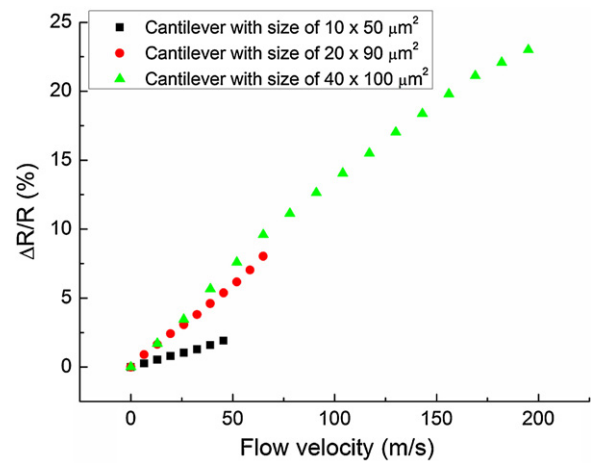


Figure 8. Plots of the piezoresistance percentage changes with respect to the flow velocity increment for cantilevers with areas of 10×50 (black curve), 20×90 (red curve) and $40 \times 100 \mu\text{m}^2$ (green curve). The length of the SiNWs is fixed to $5 \mu\text{m}$ for all cantilevers.

However, in our case, the sensitivity is not simply proportional to its area. As shown in figure 8, the percentage of the piezoresistance changes is plotted. The percentage changes are calculated by first averaging the resistance values recorded from at least three identical designs. Such an average value is normalized by the original piezoresistance measured at the initial state ($V = 0 \text{ m s}^{-1}$) in the second step. The overall

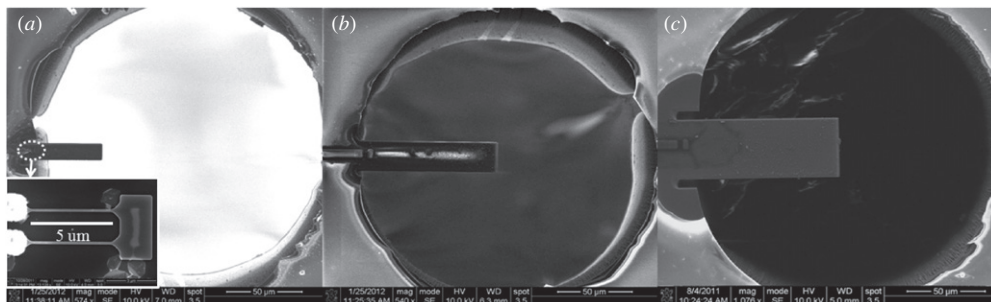


Figure 7. SEM photos of the air-flow sensor with three different cantilever sizes: 10×50 , (b) 20×90 and (c) $40 \times 100 \mu\text{m}^2$. The length of SiNWs is fixed to $5 \mu\text{m}$ in all cantilevers.

percentage changes of piezoresistance are 1.92%, 8.05% and 23% for the cantilevers with the areas of 10×50 , 20×90 and $40 \times 100 \mu\text{m}^2$, respectively. Note that these resistance changes correspond to the different sensing range due to the safety working limit of the device. As indicated in figure 8, the safe working range for the cantilever of $10 \times 50 \mu\text{m}^2$ is only up to 45 m s^{-1} . The safety working ranges for cantilevers with areas of 20×90 and $40 \times 100 \mu\text{m}^2$ are 65 and 195 m s^{-1} , respectively. In each cantilever size, the proper device working range is verified through the fatigue test, which is conducted for three cantilevers with identical size under gradually increased air flow. As a result, the working range is guaranteed without the cantilever breaking for at least three trials. To provide fair comparison among the three designs, the average piezoresistance percentage changes over flow velocity are calculated. The highest average change is $0.124\% \text{ m}^{-1} \text{ s}^{-1}$ recorded for the cantilever with an area of $20 \times 90 \mu\text{m}^2$ and the lowest change of $0.043\%/\text{m s}^{-1}$ recorded for the cantilever with a size of $10 \times 50 \mu\text{m}^2$. For the cantilever with the largest size of $40 \times 100 \mu\text{m}^2$, the average percentage change is $0.116\% \text{ m}^{-1} \text{ s}^{-1}$. With the tensile stress up to 110 MPa (equivalent to the flow velocity of 65 m s^{-1}) extracted from the simulation, the plots of resistance changes in figure 8 are in good agreement with previously reported data [60]. For the cantilever with a size of $40 \times 100 \mu\text{m}^2$, the stress extracted is up to 340 MPa (equivalent to the flow velocity of 195 m s^{-1}) and it is difficult to correlate such large stress with any reported test data. However, a similar trend of resistance percentage changes ($\Delta R/R\%$) has just been reported by Wei *et al* [61]. In their report, the slope of percentage changes ($\Delta R/R\%$) drops after reaching 15% and that is almost identical to our findings under the larger tensile stress (the green curve shown in figure 8). The slight difference is that the slope drops after $\Delta R/R$ reaches 10% in our case. This early drop of resistance change could be the combination of the piezoresistive effect under large tensile stress and the effect of the flow status changes (from the laminar to transition regime) due to the increment of flow velocity. Recall the equations of flow developing length (L_d) in section 2.1. In the turbulent regime, the developing length is much shorter than that of laminar flow. Thus, the actual L_d may become shorter even in the transition regime, which results in the deviation from the assumption for the uniform load on the cantilever. In conclusion, the cantilever with the dimensions of $20 \times 90 \mu\text{m}^2$ provides better linearity and higher average resistance percentage changes.

4.2.2. Effect of SiNW length variations on the cantilever flow sensor. After finalizing the geometry factor of the cantilever ($20 \times 90 \mu\text{m}^2$), the characterization for the length of SiNWs is done with three different variations: 2, 5 and $10 \mu\text{m}$. Figure 9 plots the piezoresistance changes with respect to the flow velocity (V) increment for designs with different lengths of SiNWs. The insets in each plot indicate the piezoresistance variations at the initial state ($V = 0 \text{ m s}^{-1}$) and final state ($V = 65 \text{ m s}^{-1}$).

As summarized in table 2, the highest average sensitivity is obtained for the $10 \mu\text{m}$ SiNW design, which is almost

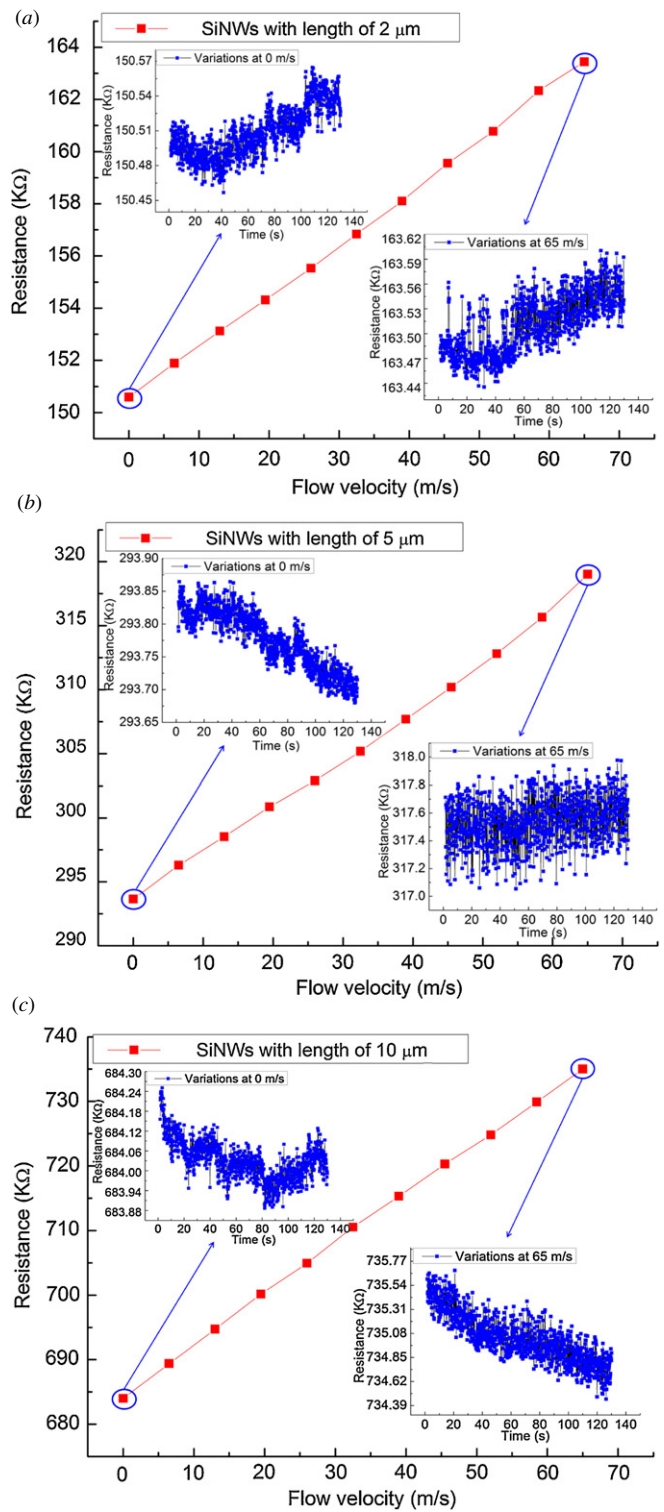


Figure 9. Plots of the piezoresistance changes with respect to the flow velocity variations for the cantilever flow sensor with the SiNW lengths of (a) 2, (b) 5 and (c) $10 \mu\text{m}$.

four times higher than that of the $2 \mu\text{m}$ SiNW design, but is still around 500Ω lower than the resistance fluctuation at the final state. An even more severe resistance fluctuation occurs in the $5 \mu\text{m}$ SiNW design and thereby both designs fail to detect the unit flow velocity change (1 m s^{-1}) due to increased flow-induced fluctuations. However, the average

Table 2. Summarized information from figure 9.

Length of SiNWs (μm)	Normalized sensitivity ($\Omega \text{ m}^{-1} \text{ s}^{-1}$)	Piezoresistance variations (Ω)		Cantilever area (μm^2)
		Initial state	Final state	
2	198	100	170	20×90
5	386	170	800	20×90
10	785	360	1250	20×90

piezoresistance change ($198 \Omega \text{ m}^{-1} \text{ s}^{-1}$) is almost 30Ω higher than its resistance fluctuation at the final state for the $2 \mu\text{m}$ SiNW design. Therefore, the air-flow-sensing resolution down to 1 m s^{-1} can be realized. According to the literature [62], the nonlinearity can be characterized by the following equation

$$L = \sqrt{\frac{\int_{X_l}^{X_u} [f(x) - g(x)]^2 dx}{X_u - X_l}}, \quad (10)$$

where L (nonlinearity) is said to be the root mean square (RMS) of the deviation of a function of the measurement curve $f(x)$ from an ideal straight line $g(x)$, and X_u and X_l correspond to upper and lower boundary conditions for a given measurement, the device nonlinearity is calculated to be around 0.1% , which is improved by an order of magnitude compared with recently reported piezoresistive cantilever flow sensor designs [47, 48]. To make a fair comparison with a recently reported flow sensor design, table 3 summarizes the sensitivity and linearity of SiNW-based cantilever flow sensors together with other recently reported piezoresistive cantilever flow sensors. As indicated in the second last column of table 3, compared with reported designs using other piezoresistive sensing elements, the SiNW-based cantilever flow sensor does significantly improve the device sensitivity. To eliminate the geometry effect for further fair comparisons, the effective sensing area of the device has also been normalized and listed in the last column of table 3.

The average percentage changes of the resistance are extracted to further analyze the sensitivity variations based on the SiNW length changes. As shown in figure 10, after a normalization of each piezoresistance at the initial state, the cantilever with $2 \mu\text{m}$ long SiNWs shows a high percentage change (8.6%). For the 5 and $10 \mu\text{m}$ SiNW designs, the percentage changes are 8.05% and 7.45% , respectively. Therefore, the trend of percentage changes is inversely proportional to the length of SiNWs and this can be explained by the gauge factor difference, which will be introduced in section 4.2.3.

Besides the less remarkable piezoresistive effect, the reported cantilever-based piezoresistive air-flow sensors also suffer poor hysteresis [46, 63]. Thus, in order to verify the air-flow-sensing consistency of our device, the repeatability test is conducted. The flow meter (shown in figure 6) is programmed with a given increasing step of 13 m s^{-1} and starting at the flow velocity of 0 m s^{-1} . The duration between each step is set to 5 s . After reaching the flow velocity of 65 m s^{-1} , the air flow is decreased back to its initial state with the same velocity-changing step and duration to complete one cycle. There two complete cycles are recorded

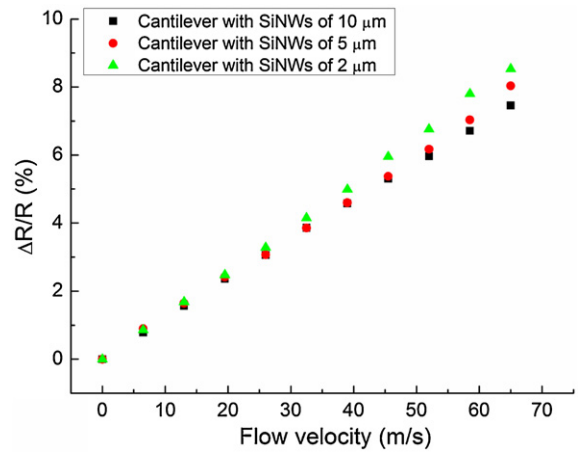


Figure 10. Plots of the piezoresistance percentage changes with respect to the flow velocity increment for cantilevers with the SiNW lengths of 10 (black curve), 5 (red curve) and $2 \mu\text{m}$ (green curve). The dimensions of the cantilever are fixed to $20 \times 90 \mu\text{m}^2$ for all designs.

over 130 s (limited by the maximum data storage capacity of the semiconductor characterization system). Results of the repeatability test are plotted on the right of figure 11 with the extracted hysteresis shown on the left. The numbers (1–4) indicated in the hysteresis plots refer to four different testing cycles plotted in the corresponding repeatability test. With a matched result of the constant flow-sensing behavior demonstrated in the repeatability test, the almost overlapped hysteresis curve is plotted for the cantilever flow sensor with $2 \mu\text{m}$ long SiNWs (shown in figure 11(a)). On the other hand, for the $5 \mu\text{m}$ SiNW design, the inconsistency is spotted during the test, especially at the region after reaching the initial state. Although the resistance is able to be restored back to almost the original value during the 10 s before starting the next cycle, such slight drifts of the original resistance are accumulated to the next test cycle and result in even larger total resistance drifts. The worst situation is recorded for the design with $10 \mu\text{m}$ SiNWs as plotted in figure 11(c). Similar to that of the $5 \mu\text{m}$ design, the resistance drifts after one complete test cycle, but unlike the $5 \mu\text{m}$ design, the piezoresistance is not able to return back to the original value at the initial state during the 10 s interval between two test cycles. For longer SiNWs, which are located relatively far away from the supporting substrate, are more subject to the mechanical movement. As a result, it is less immune to the air-flow-induced fluctuation and needs longer relaxation time for resistance to be restored. Therefore, the design with shorter SiNWs ($2 \mu\text{m}$) gives better performance in terms of the flow-sensing consistency. The same explanation may also be applied to the larger piezoresistance variations of longer SiNW designs at the final state shown in figure 9.

In summary, the cantilever flow sensor with the $2 \mu\text{m}$ SiNW design demonstrates better air-sensing capabilities in terms of sensitivity, linearity and repeatability/hysteresis. In addition, the higher gauge factor of $2 \mu\text{m}$ will also be extracted in the following part.

Table 3. Summary of device sensitivity for recently reported designs together with our designs.

References	Piezoresistive element	Cantilever area (μm^2)	Linearity %	Sensitivity ($\Omega \text{ m}^{-1} \text{ s}^{-1}$)	Normalized sensitivity ^a ($\Delta\Omega \Omega^{-1} \text{ m}^{-1} \text{ s}^{-1}$)	Normalized sensitivity ^b ($\Delta\Omega \Omega^{-1} \text{ m}^{-1} \text{ s}^{-1} \mu\text{m}^{-2}$)
Ma et al [63]	Pt resistor	400 × 4000	NA	0.0533	1.757×10^{-4}	1.1×10^{-10}
Lee et al [45]	Pt resistor	2000 × 2000 + 400 × 2000	NA	0.0785	2.243×10^{-4}	4.67×10^{-11}
Aiyar et al [46]	Conductive elastomer	1500 × 400	NA	66	2.295×10^{-4}	3.825×10^{-10}
Li et al [48]	P-doped bulk silicon wire	400 × 1100	~ 1	0.71	4.733×10^{-5}	1.08×10^{-10}
Song et al [47]	Conductive elastomer	3500 × 600	~ 1	14.5	7.25×10^{-4}	3.45×10^{-10}
2 μm SiNW design	P-doped SiNWs	20 × 90	~ 0.1	198	1.32×10^{-3}	7.33×10^{-7}
5 μm SiNW design	P-doped SiNWs	20 × 90	~ 0.4	386	1.314×10^{-3}	7.3×10^{-7}
10 μm SiNW design	P-doped SiNWs	20 × 90	~ 0.3	785	1.148×10^{-3}	6.376×10^{-7}

^a First normalization by its original piezoresistance at the initial state ($V = 0 \text{ m s}^{-1}$).

^b Based on the first normalization, the second normalization based on the different cantilever effective sensing area.

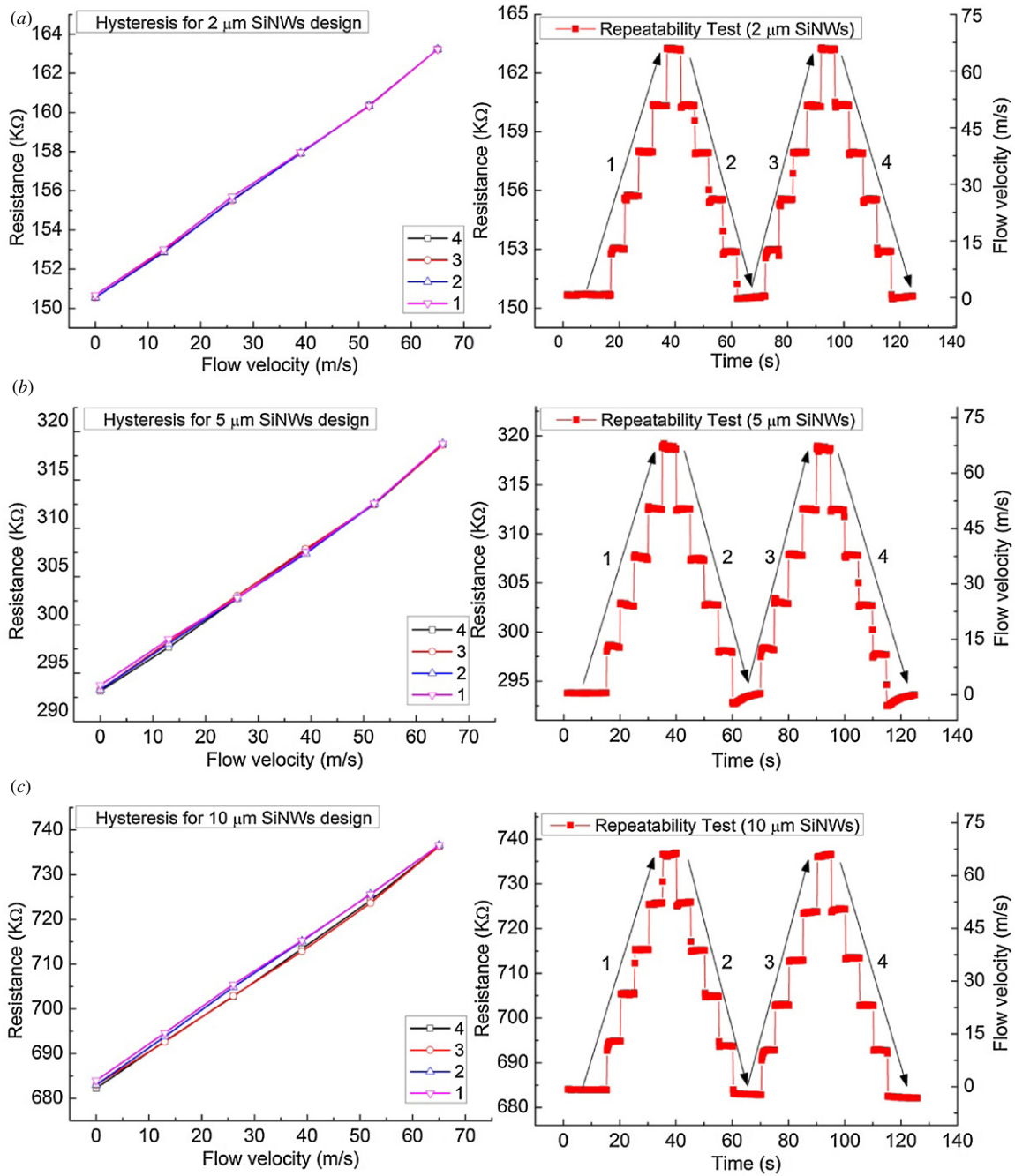


Figure 11. The repeatability/hysteresis tests for cantilever flow sensors with the SiNW lengths of (a) 2, (b) 5 and (c) 10 μm.

4.2.3. Pressure validation test and gauge factor extraction.

As mentioned previously, to verify the assumption of uniform load on the cantilever beam, a pressure regulator (ALICAT PCD series) is placed just before air flows entering the hermetic sealing base (shown in figure 6). The values of feedback air pressure are taken at four different velocity points. Meanwhile, the cantilever tip deflections are captured by a white-light interferometer (Veeco NT3300) at four corresponding air velocity moments. Meanwhile, the FEM modeling is also conducted based on the same values of four recorded air pressures. The final goal is to match cantilever tip deflections extracted from the FEM modeling to actual measurement

results under the same applied pressure in both cases. In addition, results from theoretical calculation based on equation (6) are also provided as a basic reference for comparisons. The initial tip deflection cannot be found based on the theoretical calculation from (6), but it can be estimated by applying the pre-stressed condition in the FEM modeling and the values of applied pre-stress are 150 MPa (tensile) for SiN_x and 250 MPa (compressive) for SiO₂ [64].

As tabulated in table 4, the simulation results are in good agreement with measurement results, which validates the assumption made in section 2.1. To further explore the piezoresistive effect of SiNWs, the strain (ϵ) on SiNWs with

Table 4. Comparisons of cantilever tip deflections between measurement result (captured by Veeco NT3300) and FEM result.

Pressure (Pa)	Flow velocity (m s ⁻¹)	Cantilever tip deflection (μm)		
		Veeco	FEM	Calculation
0	0	3.12	3.09	NA
13 790	13	3.48	3.47	3.44
41 360	39	4.21	4.24	4.07
68 940	65	4.95	4.99	4.69

different lengths is extracted from the FEM modeling as well. Based on the definition of gauge factor (G) given as

$$G = \frac{\frac{\Delta R}{R}}{\varepsilon}, \quad (11)$$

the average gauge factor of 75 for 2 μm SiNWs is reported. For SiNWs with lengths of 5 and 10 μm , the average gauge factors of 68 and 64 are extracted, respectively. These results are in good agreement with recently reported data [65]. In general, the gauge factor is inversely proportional to the length of SiNWs. As discussed in the previous section, the longer SiNWs stay relatively far away from the supported substrate or clamp point. From the mechanical point of view, less mechanical strain is distributed at the region away from the conjunction point, thus a smaller gauge factor.

5. Conclusion

In this paper, we first describe the flow-sensing principle in a fully developed internal boundary situation. Confined by the physical channel length, an assumption of uniformly loaded pressure on the cantilever is made and also validated by measurement results. Despite the tradeoff of slightly lower sensitivity, SiN_x is used as the passivation material due to its higher Young's modulus and the tensile range stress (compensation of initial compressive stress). In addition, with an ultralow supply voltage (0.1 V) and high piezoresistance (>150 k Ω), the power consumption of the device is dramatically reduced to be less than 1 μW . After optimization of the device geometry factor, our reported cantilever flow sensor demonstrates excellent air-flow-sensing performances in terms of the device sensitivity, linearity and repeatability/hysteresis. Compared with the recently reported designs, our SiNW-based flow sensor shows great scalability for the device dimension variation. Moreover, such a miniaturized device could be implemented in more technology-oriented biomedical applications such as a blood flow sensor. Finally, a reasonable gauge factor is extracted, which is in good agreement with the value recently reported in the literature.

Acknowledgments

This work was supported by grants from Academic Research Committee (ARC) Fund MOE2009-T2-2-011 (R-263000598112) at the National University of Singapore; A*STAR, SERC under grant nos 1021650084, 1021010022

and 1021520013; A*STAR, SERC funded project 'Development of wearable micro blood flow sensors for livestock breeding'; and NRF CRP funded project 'self-powered body sensor network for disease management and prevention-oriented healthcare'.

References

- [1] Shikida M, YoshiKawa K, Iwai S and Sato K 2012 Flexible flow sensor for large-scale air-conditioning network systems *Sensors Actuators A* doi: [10.1016/j.sna.2011.12.002](https://doi.org/10.1016/j.sna.2011.12.002)
- [2] Li C, Wu P-M, Hartings J A, Wu Z, Ahn C H, LeDoux D, Shutter L A and Narayan R K 2011 Smart catheter flow sensor for real-time continuous regional cerebral blood flow monitoring *Appl. Phys. Lett.* **99** 233705
- [3] Shikida M, Yokota T, Kawabe T, Funaki T, Matsushima M, Iwai S, Matsunaga N and Sato K 2010 Characteristics of an optimized catheter-type thermal flow sensor for measuring reciprocating airflows in bronchial pathways *J. Micromech. Microeng.* **20** 125030
- [4] Billat S, Kliche K, Gronmaier R, Nommensen P, Auber J, Hedrich F and Zengerle R 2008 Monolithic integration of micro-channel on disposable flow sensors for medical applications *Sensors Actuators A* **145-146** 66-74
- [5] Van Putten A F P and Middelhoek S 1974 Integrated silicon anemometer *Electron. Lett.* **10** 425-6
- [6] Haasl S and Stemme G 2008 *Comprehensive Microsystems* ed Z Hans (Oxford: Elsevier) pp 209-72
- [7] Buchner R, Froehner K, Sosna C, Benecke W and Lang W 2008 Toward flexible thermoelectric flow sensors: a new technological approach *J. Microelectromech. Syst.* **17** 1114-9
- [8] van Oudheusden B W and van Herwaarden A W 1989 High-sensitivity 2-D flow sensor with an etched thermal isolation structure *Sensors Actuators A* **22** 425-30
- [9] Neda T, Nakamura K and Takumi T 1996 A polysilicon flow sensor for gas flow meters *Sensors Actuators* **54** 626-31
- [10] Nguyen N T 1997 Micromachined flow sensors—a review *Flow Meas. Instrum.* **8** 7-16
- [11] Buchner R, Sosna C, Maiwald M, Benecke W and Lang W 2006 A high-temperature thermopile fabrication process for thermal flow sensors *Sensors Actuators A* **130-131** 262-6
- [12] Sosna C, Walter T and Lang W 2011 Response time of thermal sensor with air as fluid *Sensors Actuators A* **172** 15-20
- [13] Tabata O 1986 Fast-response silicon flow sensor with an on-chip fluid temperature sensing element *IEEE Trans. Electron Devices* **33** 361-5
- [14] Tai Y C and Muller R S 1988 Lightly-doped polysilicon bridge as a flow meter *Sensors Actuators* **15** 63-75
- [15] Lofdahl L, Stemme G and Johansson B 1989 A sensor based on silicon technology for turbulence measurements *J. Phys. E: Sci. Instrum.* **22** 391-3
- [16] Stemme G N 1986 A monolithic gas flow sensor with polyimide as thermal insulator *IEEE Trans. Electron Devices* **33** 1470
- [17] Liu C, Huang J B, Zhu Z J, Jiang F K, Tung S, Tai Y C and Ho C M 1999 A micromachined flow shear-stress sensor based on thermal transfer principles *J. Microelectromech. Syst.* **8** 90-9
- [18] Xu Y, Lin Q, Lin G Y, Katragadda R B, Jiang F K, Tung S and Tai Y C 2005 Micromachined thermal shear-stress sensor for underwater applications *J. Microelectromech. Syst.* **14** 1023-30
- [19] Xu Y, Chiu C W, Jiang F K, Lin Q and Tai Y C 2005 A MEMS multi-sensor chip for gas flow sensing *Sensors Actuators A* **121** 253-61

- [20] Kim S, Nam T and Park S 2004 Measurement of flow direction and velocity using a micromachined flow sensor *Sensors Actuators A* **114** 312–8
- [21] Shin W C and Besser R S 2006 A micromachined thin-film gas flow sensor for microchemical reactors *J. Micromech. Microeng.* **16** 731–41
- [22] Tan Z Y, Shikida M, Hirota M, Sato K, Iwasaki T and Iriye Y 2007 Experimental and theoretical study of an on-wall in-tube flexible thermal sensor *J. Micromech. Microeng.* **17** 679–86
- [23] Ahrens R and Schlote-Holubek K 2009 A micro flow sensor from a polymer for gases and liquids *J. Micromech. Microeng.* **19** 074006
- [24] Kliche K, Billat S, Hedrich F, Ziegler C and Zengerle R 2011 Sensor for gas analysis based on thermal conductivity, specific heat capacity and thermal diffusivity *Proc. 24th Int. Conf. on Micro Electro Mechanical Systems (MEMS)* pp 1189–92
- [25] Wang Y H, Chen C P, Chang C M, Lin C P, Lin C H, Fu L M and Lee C Y 2009 MEMS-based gas flow sensors *Microfluids Nanofluids* **6** 333–46
- [26] Svedin N, Kälvesten E and Stemme G 2003 A lift force sensor with integrated hot-chips for wide range flow measurements *Sensors Actuators A* **109** 120–30
- [27] Svedin N, Kälvesten E, Stemme E and Stemme G 1998 A new silicon gas-flow sensor based on lift force *J. Microelectromech. Syst.* **7** 303–8
- [28] Shajii J, Ng K Y and Schmidt M A 1992 A microfabricated floating-element shear stress sensor using wafer-bonding technology *J. Microelectromech. Syst.* **1** 89–94
- [29] Barlian A A, Park S-J, Mukundan V and Pruitt B L 2007 Design and characterization of microfabricated piezoresistive floating element-based shear stress sensors *Sensors Actuators A* **134** 77–87
- [30] Ozaki Y, Ohyama T, Yasuda T and Shimoyama I 2000 An air flow sensor modeled on wind receptor hairs of insects *Proc. 13th Int. Conf. on Micro Electro Mechanical Systems (MEMS)* pp 531–6
- [31] van der Wie A J, Boillat M A and de Rooij N F 1995 A Bi-directional silicon orifice flow sensor characterised for fluid temperature and pressure *8th Int. Conf. on Solid-State Sensors and Actuators and Eurosensors IX* vol 2, pp 420–3
- [32] Chen J, Fan Z F, Zou J, Engel J and Liu C 2003 Two-dimensional micromachined flow sensor array for fluid mechanics studies *J. Aerosp. Eng.* **16** 85–97
- [33] Liu J, Wang J and Li X 2012 Fully front-side bulk-micromachined single-chip micro flow sensors for bare-chip SMT (surface mounting technology) packing *J. Micromech. Microeng.* **22** 035020
- [34] Lee C, Itoh T and Suga T 1996 Micromachined piezoelectric force sensors based on PZT thin films *IEEE Trans. Ultrason. Ferroelectr. Freq. Control* **43** 553–9
- [35] Zhang S, Lou L and Lee C 2012 Piezoresistive nanowire based nanoelectromechanical system cantilever air flow sensor *Appl. Phys. Lett.* **100** 023110
- [36] Lee C, Thillaigovindan J, Chen C-C, Chen X T, Chao Y-T, Tao S H, Xiang W F, Yu A, Feng H H and Lo G Q 2008 Si nanophotonics based cantilever sensor *Appl. Phys. Lett.* **93** 113113
- [37] Seo Y H and Kim B H 2010 A self-resonant micro flow velocity sensor based on a resonant frequency shift by flow-induced vibration *J. Micromech. Microeng.* **20** 075024
- [38] Lee Y-T, Lin C-W, Lin C-M, Yeh S-R, Chang Y-C and Fang W 2010 A pseudo-3D glass microprobe array: glass microprobe with embedded silicon for alignment and electrical interconnection during assembly *J. Micromech. Microeng.* **20** 025014
- [39] Li Y, Zheng Q, Hu Y and Xu Y 2011 Micromachined piezoresistive accelerometers based on an asymmetrically gapped cantilever *J. Microelectromech. Syst.* **20** 83–94
- [40] Liu H, Tay C J, Quan C, Kobayashi T and Lee C 2011 Piezoelectric MEMS energy harvester for low-frequency vibrations with wideband operation range and steadily increased output power *J. Microelectromech. Syst.* **20** 1131–42
- [41] Su Y, Evans A G R, Brunnschweiler A and Ensell G 2002 Characterization of a highly sensitive ultra-thin piezoresistive silicon cantilever probe and its application in gas flow velocity sensing *J. Micromech. Microeng.* **12** 780–5
- [42] Fan Z F, Chen J, Zou J, Bullen D, Liu C and Delcomyn F 2002 Design and fabrication of artificial lateral line flow sensors *J. Micromech. Microeng.* **12** 655–61
- [43] Chen N N, Tucker C, Engel J M, Yang Y C, Pandya S and Liu C 2007 Design and characterization of artificial haircell sensor for flow sensing with ultrahigh velocity and angular sensitivity *J. Microelectromech. Syst.* **16** 999–1014
- [44] Wang Y H, Lee C Y and Chiang C M 2007 A MEMS-based air flow sensor with a free-standing micro-cantilever structure *Sensors* **7** 2389–401
- [45] Lee C Y, Wen C Y, Hou H H, Yang R J, Tsai C H and Fu L M 2009 Design and characterization of MEMS-based flow-rate and flow-direction microsensors *Microfluids Nanofluids* **6** 363–71
- [46] Aiyar A R, Song C, Kim S-H and Allen M G 2009 An all-polymer airflow sensor using a piezoresistive composite elastomer *Smart Mater. Struct.* **18** 115002
- [47] Song C, Aiyar A R, Kim S-H and Allen M G 2011 Exploitation of aeroelastic effects for drift reduction, in an all-polymer air flow sensor *Sensors Actuators A* **165** 66
- [48] Li D, Zhao T, Yang Z C and Zhang D C 2010 Monolithic integration of a micromachined piezoresistive flow sensor *J. Micromech. Microeng.* **20** 035024
- [49] Reck K, Richter J, Hansen O and Thomsen E V 2008 Piezoresistive effect in top-down fabricated silicon nanowires *Proc. IEEE MEMS* pp 717–20
- [50] Barlian A A, Park W-T, Mallon J R, Rastegar A J and Pruitt B L 2009 Review: semiconductor piezoresistance for microsystems *Proc. IEEE* **97** 513–52
- [51] Toriyama T, Tanimoto Y and Sugiyama S 2002 *J. Microelectromech. Syst.* Single crystal silicon nano-wire piezoresistors for mechanical sensors **11** 605–11
- [52] Milne J S, Rowe A C H, Arscott S and Renner C 2010 Giant piezoresistance effects in silicon nanowires and microwires *Phys. Rev. Lett.* **105** 206802
- [53] Singh P, Miao J M, Park W-T and Kwong D-L 2011 Gate-bias-controlled sensitivity and SNR enhancement in a nanowire FET pressure sensor *J. Micromech. Microeng.* **21** 105007
- [54] Lou L, Park W-T, Zhang S, Lim L, Kwong D-L and Lee C 2011 Characterization of silicon nanowire embedded in a MEMS diaphragm structure within large compressive strain range *IEEE Electron Device Lett.* **32** 1764–6
- [55] White F M 1999 *Fluid Mechanics* 4th edn (New York: McGraw-Hill)
- [56] Bansal R K 2010 *A Textbook of Strength of Materials* 4th edn (New Delhi: Laxmi Publications) revised
- [57] Knight J, McLean J and Degertekin F L 2004 Low temperature fabrication of immersion capacitive micromachined ultrasonic transducers on silicon and dielectric substrates *IEEE Trans. Ultrason. Ferroelectr. Freq. Control* **51** 1324–33
- [58] Yang J, Gaspar J and Paul O 2008 Fracture properties of LPCVD silicon nitride and thermally grown silicon oxide

- thin films from the load-deflection of long Si₃N₄ and SiO₂/Si₃N₄ diaphragms *J. Microelectromech. Syst.* **17** 1120–34
- [59] Kanda Y 1982 A graphical representation of the piezoresistance coefficients in silicon *IEEE Trans. Electron Devices* **29** 64–70
- [60] Toriyama T, Funai D and Sugiyama S 2003 Piezoresistance measurement on single crystal silicon nanowires *J. Appl. Phys.* **93** 561
- [61] Wei J, Magnani S and Sarro P 2012 Suspended submicron silicon-beam for high sensitivity piezoresistive force sensing cantilevers *Sensors Actuators A* doi: <http://dx.doi.org/10.1016/j.sna.2012.02.021>
- [62] Emancipator K and Kroll M 1993 A quantitative measure of nonlinearity *Clin. Chem.* **39** 766–72
- [63] Ma R H, Lee C Y, Wang Y H and Chen H J 2008 Microcantilever-based weather station for temperature, humidity and flow rate measurement *Microsyst. Technol.* **14** 971
- [64] Tarraf A, Daleiden J, Irmer S, Prasai D and Hillmer H 2004 Stress investigation of PECVD dielectric layers for advanced optical MEMS *J. Micromech. Microeng.* **14** 317–23
- [65] Barwicz T, Klein L, Koestor S J and Hamann H 2010 Silicon nanowire piezoresistance: impact of surface crystallographic orientation *Appl. Phys. Lett.* **97** 023110